Nano Research

Open Access

Research Article

High-performance flexible Sb_2Se_3 thin-film photodetector for tunable color imaging and wearable physiological monitoring applications

Shuo Chen[1], Hong-Bo Li[1], Yi Fu[1], Guo-Qiang Liu[2], Muhammad Ishaq[1], Jun Luo[3], Jian-Min Li[3], Bo Che[4], Jing-Ting Luo[1], Liming Ding[5] ✉, Tao Chen[4] ✉, and Guang-Xing Liang[1] ✉

[1] *Shenzhen Key Laboratory of Advanced Thin Films and Applications, Key Laboratory of Optoelectronic Devices and Systems of Ministry of Education and Guangdong Province, State Key Laboratory of Radio Frequency Heterogeneous Integration, College of Physics and Optoelectronic Engineering, Shenzhen University, Shenzhen 518060, China*
[2] *The Hospital of Shenzhen General Station of Exit and Entry Frontier Inspection, Shenzhen 518024, China*
[3] *Key Laboratory of Artificial Micro- and Nano-structures of Ministry of Education, School of Physics and Technology, Wuhan University, Wuhan 430072, China*
[4] *Hefei National Research Center for Physical Sciences at Microscale, CAS Key Laboratory of Materials for Energy Conversion, Department of Materials Science and Engineering, University of Science and Technology of China, Hefei 230026, China*
[5] *Center for Excellence in Nanoscience (CAS), Key Laboratory of Nanosystem and Hierarchical Fabrication (CAS), National Center for Nanoscience and Technology, Beijing 100190, China*

Cite this article: *Nano Research*, **2025**, *18*, 94907159. https://doi.org/10.26599/NR.2025.94907159

ABSTRACT: Antimony selenide (Sb_2Se_3) has recently made considerable advancements in photovoltaic, photoelectrochemical, and photodetector research scenarios, owing to its advantageous material merits and superior optoelectronic properties. By contrast, the exploration of flexible Sb_2Se_3 photoelectric devices are less attempted, though it possesses unique one-dimensional (1D) crystal structure to enable large deformation tolerance. Here, we develop a flexible Sb_2Se_3 thin-film photodetector on polyimide substrate. Thanks to the high-quality Sb_2Se_3 light absorber and benign interfaces at both back contact and heterojunction regions, the carrier dynamics are effectively optimized. The leading flexible Sb_2Se_3 photodetector showcases self-powered and broadband features, with exceptional responsivity of 0.51 $A\cdot W^{-1}$ and realistic detectivity up to 1.32 × 10^{13} Jones, ultra-fast response speed of 49 ns/351 ns of rise and decay times, and remarkable mechanical deformation stability, flourishing the high-level development for flexible Sb_2Se_3 photodetectors. Interestingly, a tunable single/dual-color flexible imaging system under band alignment modulation, along with a wearable and accurate heart rate/arterial blood oxygen saturation photoplethysmography detection system highlights the great application potential for flexible Sb_2Se_3 photodetectors.

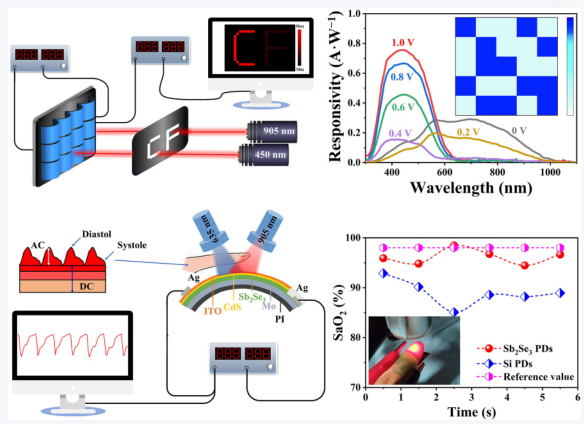

KEYWORDS: Sb_2Se_3, flexible thin-film photodetector, color imaging, heart rate, arterial blood oxygen saturation

1 Introduction

Photodetectors are capable of converting optical signals or other electromagnetic radiation into electrical signals and serve as a cornerstone in various imaging and sensing applications [1–3]. Currently, silicon (Si) and III-V compounds are the most common crystalline inorganic semiconductors used in visible (Vis) and near-infrared (NIR) photodetectors [4, 5]. However, the application needs in wearable or implantable optoelectronic devices cannot be fulfilled because of their rigid constructions, brittleness, and complex production procedures. Thus, there is a need for alternative candidates that can be compatible with deformable

Received: October 20, 2024; **Revised:** November 21, 2024
Accepted: November 26, 2024

✉Address correspondence to Liming Ding, ding@nanoctr.cn; Tao Chen, tchenmse@ustc.edu.cn; Guang-Xing Liang, lgx@szu.edu.cn

substrates and adhering to the standards of low-cost manufacturing towards high-performance flexible photodetectors. Antimony selenide (Sb_2Se_3) is a single stable orthorhombic compound belonging to the V-VI group, characterized by a low melting temperature (~ 885 K), low crystallization temperature (~ 400 K), and high vapor pressure (~ 1200 Pa at 825 K) [6–9]. These properties enable the effective preparation of Sb_2Se_3 absorber layer on flexible substrates using various vacuum deposition methods [10–12]. Sb_2Se_3 exhibits a broad spectral response spanning from ultraviolet (UV) to NIR, accompanied with substantial absorption coefficient (> 10^5 cm^{-1} in the visible light region) [13], a favorable carrier mobility (~ 15 $cm^2 \cdot V^{-1}$) and an excellent carrier recombination lifetime (~ 70 ns), in terms of optoelectronic properties [14–16]. Furthermore, Sb_2Se_3 showcases superior deformation tolerance thanks to its unique one-dimensional (1D) crystal structure, which endows it more appropriate for flexible application scenarios [8]. Specifically, its theoretical fracture strain as high as 28% is much superior to that of 17% for Si [14]. Consequently, there are high expectations for achieving high-performance flexible Sb_2Se_3-based photodetectors.

Over the past decade, there has been significant progress and breakthroughs in the research of Sb_2Se_3 photodetectors [6, 9, 15–17]. It began with the reports of photoconductive-type Sb_2Se_3 photodetectors based on 1D nanostructures such as nanowires, nanorods, or stacked thin films, and has since developed into self-powered photovoltaic-type thin-film photodetectors due to their significant potential value. By contrast, the research efforts of flexible Sb_2Se_3 photodetectors are less attempted. The initial few reports of flexible Sb_2Se_3 nanowire photodetectors based on polyethylene terephthalate (PET) substrates exhibited considerable response to visible light with excellent flexibility and durability [18, 19]. Nevertheless, these photoconductive-type nanowire photodetectors were operated using external bias voltage, limiting the applications in some long-term and/or space-constrained operational environments. Until 2020, Tang et al. introduced a Sb_2Se_3-based photodiode with flexible polyimide (PI) as substrate, which could work at 0 V bias under the existence of built-in electric field, accompanied with 0.42 $A \cdot W^{-1}$ photoresponsivity and 95 dB linear dynamic range, as well as high flexibility to tolerate 69° bending angle and 1000× bending cycles [14]. Recently, Wen et al. proposed the growth of Sb_2Se_3 film with preferential [001]-orientation for a self-powered flexible photodiode, exhibiting good folding endurance, a specific detectivity of 5.1 × 10^{13} Jones, and rise/decay time of 0.16 ms /0.15 ms under NIR light irradiation [20]. Despite these endeavors, the flexible Sb_2Se_3 photodetector performance is still inferior to its rigid counterpart, e.g., concurrently extraordinary responsivity of 0.9 $A \cdot W^{-1}$ at 11 $nW \cdot cm^{-2}$, remarkable realistic detectivity of 4.78 × 10^{12} Jones determined by total noise, and rapid response regarding rise/decay time of 24 ns/75 ns for Glass/Mo/Sb_2Se_3/CdS (Al)/ITO/Ag thin-film photodetector, as reported by our group [17]. Thus, more exploration efforts concentrating on flexible thin film growth and overall carrier dynamics optimization are needed for the performance improvement of flexible Sb_2Se_3 photodetectors.

In addition, flexible photodetectors present great applications as wearable electronic devices, foldable displays, portable image sensors, biomedicine and aerospace engineering that need special requirements of flexibility, lightweight and mechanical stability. Up to now, there are only a few reports regarding heart rate detection under transmitted light-emitting diode (LED) light operation mode when using flexible Sb_2Se_3 photodetector as the detector and was worked on the outside of the finger [14]. Actually, considering its advantageous material merits and device performance, the translation of the outstanding performance and broad spectral response of the flexible Sb_2Se_3 photodetectors into practical applications and even commercial values in the market is an area that requires further exploration.

In this study, we develop a flexible photovoltaic-type photodetector utilizing a sputtered and selenized Sb_2Se_3 light absorber layer deposited on flexible PI substrate in conjunction with chemically bath deposited CdS buffer layer. This protype photodetector has demonstrated exceptional performance, boasting a high responsivity of 0.51 $A \cdot W^{-1}$, realistic detectivity up to 1.32 × 10^{13} Jones, and impressively fast response speed with rise and decay times of 49 and 351 ns. It also delivers excellent folding endurance with large bending curvature and thousands of bending cycles. Interestingly, this flexible photodetector exhibits a unique capability to convert dual-color images into single-color images effortlessly under an additional small bias voltage, meeting the demands of innovative imaging display and identification detection. Furthermore, it has the capacity to measure heart rate and arterial blood oxygen saturation, transcending the trade-offs typically associated with conventional rigid Si photodetectors, particularly in terms of achieving both high detection accuracy and environmental adaptability. These attributes hold promise for a broad array of applications, such as flexible imaging electronics and wearable physiological monitoring detectors.

2 Results and discussion

2.1 Device performance of the flexible Sb_2Se_3 thin-film photodetector

Figure 1(a) demonstrates the device configuration and working schematic of the as-fabricated flexible Sb_2Se_3 thin-film photodetector. A representative scanning electron microscope (SEM) cross-sectional image (Fig. 1(b)) signifies an evident layer-by-layer structure with thickness of approximately 1150, 80, and 250 nm for p-type Sb_2Se_3 light absorber layer, n-type CdS buffer layer, and ITO window layer, respectively. The interfaces between ITO and CdS, Sb_2Se_3 and CdS, and Sb_2Se_3 and Mo exhibit well-adherent and pinhole-free features. It will be very advantageous to suppress the current leakage and charge carrier recombination, making the device highly promising for flexible applications. Furthermore, Sb_2Se_3 exhibits unusual inherent 1D crystal structure, i.e., the $(Sb_4Se_6)_n$ ribbons are connected by weak van der Waals (vdW) forces along the *a*-axis and *b*-axis directions, while strong covalent bonding along *c*-axis direction, as illustrated by the dashed red lines in Fig. 1(c) [14]. The high-angle annular dark field scanning transmission electron microscope (HAADF-STEM) image obtained from the bulk region of Sb_2Se_3 clearly shows $(Sb_4Se_6)_n$ nanoribbons stacked in parallel in the [001] direction (Fig. S1 in the Electronic Supplementary Material (ESM)), confirming 1D structure of the sputtered and selenized Sb_2Se_3 thin film in this work. Thus, it can tolerate large deformation when properly aligning the Sb_2Se_3 film to preferential [*hk*1] orientations on flexible substrate, and is thought to provide distinct advantages in a variety of flexibility applications, e.g., flexible photodetectors. Figure 1(d) shows the monochromatic wavelength-dependent spectral responsivity (*R*) and specific detectivity (D^*) of the flexible

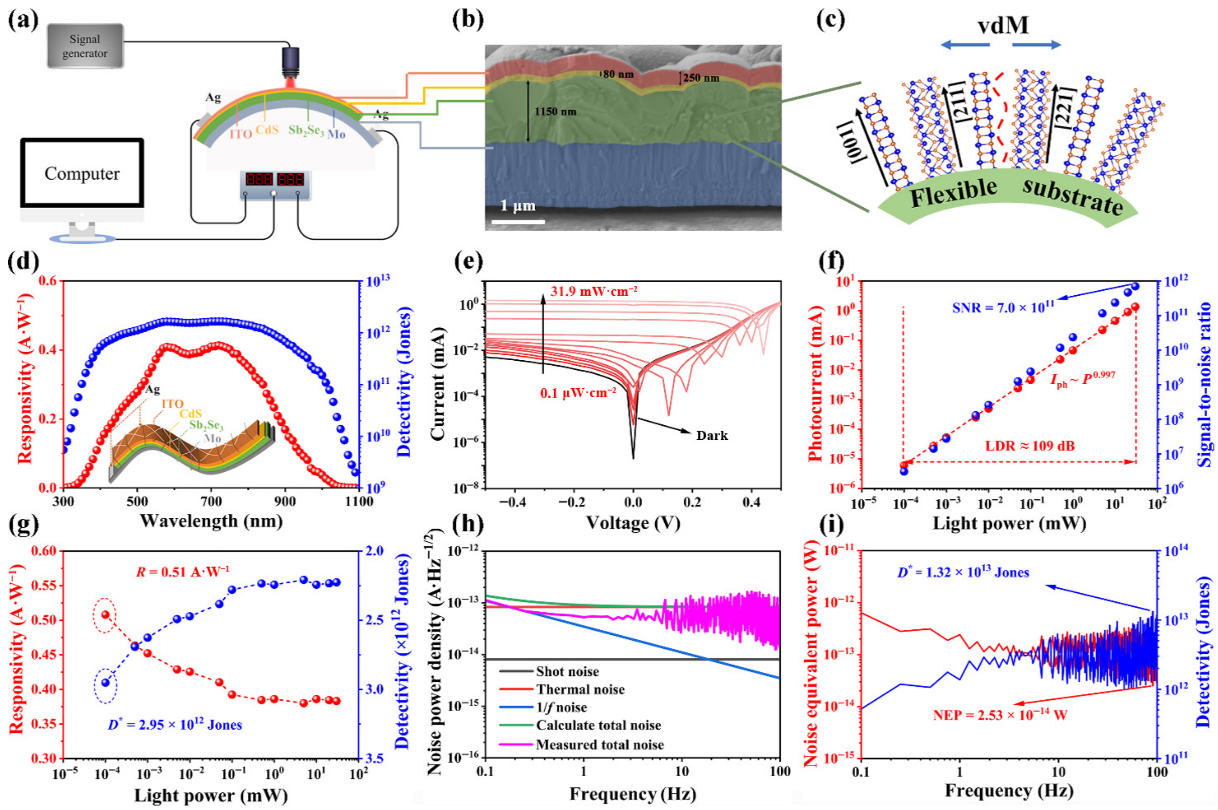

Figure 1 Photodetection performance of the flexible Sb_2Se_3 thin-film photodetector. (a) Schematic illustration of the photo-response measurements as well as a structure diagram of the flexible PI/Mo/Sb_2Se_3/CdS/ITO/Ag photodetector. (b) Cross-sectional SEM image of the flexible photodetector. (c) Large deformation tolerance for [*hk*1]-oriented Sb_2Se_3 on flexible substrate. The red dash line marks the gap between $[Sb_4Se_6]_n$ ribbons. (d) Wavelength-dependent responsivity and detectivity of the flexible photodetector, and a device configuration (inset). (e) Semilogarithmic current–voltage (*I*–*V*) curves of the flexible photodetector under 635 nm laser irradiation and dark condition. (f) The incident light power related output photocurrent and signal-to-noise ratio. (g) The incident light power dependent photodetector responsivity and specific detectivity. (h) Measured noise of the flexible photodetector, and the calculated shot noise, flicker 1/*f* noise, thermal noise, and total noise as a function of frequency. (i) Plots of the device noise equivalent power and realistic detectivity as a variation of frequency.

PI/Mo/Sb_2Se_3/CdS/ITO/Ag photodetector. Wherein, *R* values were calculated according to the equation below [21]:

$$R = \frac{I_{ph}}{P \times S} = \frac{I_{light} - I_{dark}}{P \times S} \tag{1}$$

where I_{ph} is photocurrent, i.e., the value of light current minus dark current ($I_{light} - I_{dark}$), *P* symbolizes the incident light density, *S* denotes the active device area. *R* curve demonstrates an abrupt increase at $\lambda > 350$ nm, a turning point at λ of 520 nm (corresponds to the start of CdS absorption), a plateau with *R* value exceeding 0.4 A/W from 600 to 800 nm, and eventually cut-off at 1050 nm. The broad UV–Vis–NIR spectral response indicates that this photodetector can function under a wide spectral range to broaden its scope of applications. The semilogarithmic current–voltage (*I*–*V*) curves under 635 or 905 nm laser irradiation are displayed in Fig. 1(e) and Fig. S2 in the ESM, respectively. Under laser light illumination, the photodetector demonstrates self-powered operation ability, thanks to the built-in electric field formed at Sb_2Se_3/CdS heterojunction interface, enabling the automatic separation of photo-generated electrons and holes without external power source. With increasing the incident light intensity, the current shows a synchronous increase, echoing its high responsivity. To better understand this variation, connections between photocurrent I_{ph}, signal-to-noise ratio (SNR), and linear dynamic range (LDR) under illumination power (P_0) in the range of 10^{-7}–10^{-2} W were further investigated, as plotted in Fig. 1(f), which were determined according to the following equations [22–24]:

$$I_{ph} = CP_0^{\theta} \tag{2}$$

$$\mathrm{SNR} = \frac{I_{signal}}{I_{noise}^{0}} \tag{3}$$

$$\mathrm{LDR} = 20\lg(P_{max}/P_{min}) \tag{4}$$

where θ is an index that relates to physical processes involving generation, separation, and recombination of electron–hole pairs, and *C* can be a constant at a specific wavelength. I_{signal} represents the light-activated signal current (i.e., I_{light}), and I_{noise}^{0} is the limit noise current (i.e., equals to the root-mean-square dark current I_{rms}, as described in Note S1 and Fig. S3(a)) in the ESM. P_{max} and P_{min} represent the maximum and minimum light power inside linear evolution region. Consequently, the quasi-linear variation between I_{ph} and P_0 gives an ideal θ value of 0.997, suggesting proficient generation of charge carriers from the harvested photoflux, and suppressed recombination under low trap states. LDR of 109 dB and highest SNR of 7.0×10^{11} can also be obtained, endorsing exceptional photo-response characteristics over a broad range of light intensity. Additionally, thanks to the high-quality Sb_2Se_3 absorber layer and the superior device interfaces, the lowest-detectable light intensity in the self-powered state is about

27 pW, designated by electronic noise measurement with derived I_{rms} of 1.99 pA (Fig. S3(b) in the ESM), thus, the assessed LDR stretches to 180 dB and surpasses the 160 dB LDR belonging to commercial rigid Si photodetector [25]. The red scatter point line curves in Fig. 1(g) and Fig. S4 also show the calculated light intensity dependent R, demonstrating highest R value of 0.51 A·W^{-1} (at 635 nm, 10^{-4} mW light illumination) and 0.28 A·W^{-1} (at 905 nm, 10^{-2} mW light illumination), respectively, which is comparable to that of high-performance rigid Sb_2Se_3 photodetectors. Such interesting results also indicates its extreme weak light response in both Vis and NIR regions, presenting remarkable R values at weak light intensity under limited charge carrier scattering, suppressed carrier recombination rate, and lengthened carrier lifetime. To specifically evaluate this merit, an important indicator of D^* was calculated [26, 27]:

$$D^* = \frac{\sqrt{S\Delta f}}{\text{NEP}} \tag{5}$$

$$\text{NEP} = \frac{\sqrt{I^2_{\text{noise}}}}{R} \tag{6}$$

where NEP signifies noise equivalent power, Δf is electronic bandwidth. I_{noise} is the total noise measured through a fast Fourier transform of the current versus time, herein, can be determined as 5.71 × 10^{-14} A·Hz$^{-1/2}$ (Fig. S5 in the ESM). The wavelength dependent and light power dependent D^* are displayed in Figs. 1(d) and 1(g), confirming its broadband and decent weak light detection ability. To further strengthen its authenticity, the frequency-dependent noise, NEP and D^* were also examined. Generally, the total noise of a photodetector involves shot noise (i_{shot}), flicker $1/f$ noise ($i_{1/f}$) and thermal noise ($i_{thermal}$), and the calculated total noise (i_{noise}) can be determined by [17, 26, 28, 29]:

$$\begin{cases} \langle I^2_{\text{shot}} \rangle = 2qI_{\text{dark}}\Delta f \\ \langle i^2_{1/f} \rangle = CI^{\beta}_{\text{dark}}/f^{\alpha}\Delta f \\ \langle i^2_{\text{thermal}} \rangle = \dfrac{4kT\Delta f}{R_{\text{shunt}}} \\ \langle i^2_{\text{noise}} \rangle = \langle i^2_{\text{shot}} \rangle + \langle i^2_{1/f} \rangle + \langle i^2_{\text{thermal}} \rangle \end{cases} \tag{7}$$

where q, f, T, and R_{shunt} are the elementary charge, operating frequency, absolute temperature, and shunt resistance, respectively, while C, k, α and β are the constants. As shown in Fig. 1(h), the measured noise I_{noise} is well-matched with the calculated noise i_{noise}. In addition, the flicker $1/f$ noise caused by carrier scattering contributes the main noise at lower frequency, however, the thermal noise caused by free carrier thermal motion contributes the main noise at higher frequency, leading the absence of discernible knee point within the measured frequency range [30]. Finally, the optimal realistic NEP can be as low as 2.53 × 10^{-14} W, accompanied with remarkable realistic D^* of 1.32 × 10^{13} Jones at a frequency approaching to 100 Hz, which is really competitive to those of state-of-the-art photodetectors [31, 32].

One of the important requirements for flexible photodetectors is to maintain its original performance in the condition of bending. Flexibility of the flexible Sb_2Se_3 photodetector was first examined under diverse bending curvature using a vernier caliper. The marked bending curvature radius (r_c) and the temporal current response (under 636 nm laser illumination) under different R_c conditions are portrayed in Figs. 2(a) and 2(b), respectively. The quasi-overlapped response curves reveal a trifling variation in a wide bending curvature range, i.e., from initial state (r_c = 10 mm) to large angle bending (r_c = 4 mm). To further highlight its considerable flexibility, the transient photocurrent response as a function of bending cycles under a fixed bending r_c of 4 mm is also explicitly elucidated in Fig. 2(c). After being repeated periodic on/off cycles (e.g., 1000, 2000, and 5000 cycles), the device delivers a good repeatability of the photocurrent generation. Thus, analyzing the normalized current evolution, when the bending curvature radius r_c is larger than 4 mm and bending cycles is fewer than 5000, this flexible Sb_2Se_3 photodetector can achieve exceptional adaptability and flexibility (Fig. 2(d)). To unveil the mechanism of this superior behavior, further calculation analysis is implemented. Actually, the strain of the thin-film photodetector is closely related to the bending curvature (θ_c) (inset in Fig. 2(e)). The θ_c-dependent strain was calculated through neutral axis concept by taking the Young's modulus and thickness of each layer into consideration (Note S2 in the ESM outlined the detailed calculation process). The strain of the device is smaller than 0.16% and the strain of Sb_2Se_3 is less than 0.11% in a wide θ_c range of 0° to 90°, as highlighted in Fig. 2(e). Literature shows a failure stress of 7.12 N·m^{-1} along the c-axis direction for Sb_2Se_3, which is approximately 7 times higher than the value (1.02 N·m^{-1}) along the a-axis direction [13]. The failure strain strength values (11% along c-axis and 28% along a-axis) are significantly higher than the strain of the device observed in Fig. 2(e) (less than 0.16%). Importantly, such strain is situated in typical elastic strain region, inferring the stress–strain practically obeys the Hooke law and the strain can perfectly retain even after thousands folding cycles. Afterwards, the operational stability of the flexible Sb_2Se_3 photodetector was also examined at temperatures of 100, −50 °C, and in indoor storage for one month. A similar light response can be witnessed under multiple light on/off cycles, and hardly any changes between the dark and light currents are observed (Fig. 2(f)), indicating reliable operation stability and opening up a promising path to withstand some challenging application environments. Finally, the device response speed is a crucial performance metric as it dictates its capability to effectively track a fast-changing optical signal. Under a pulse laser irradiation with pulse duration of 3–5 ns, the realistic rise time and decay time are determined to be 49 and 351 ns for the flexible Sb_2Se_3 photodetector at zero bias, respectively. These times are significantly shorter than those of previously reported flexible Sb_2Se_3 photodetectors [14, 20, 33]. Overall, Table 1 summarizes the key device performance parameters, as well as a comparison to the literature reported Sb_2Se_3 flexible photodetectors, and the representative silicon, PbS quantum dots, graphene, 2D semiconductors, perovskite, and organic flexible devices [14, 20, 25, 30, 33–38]. Importantly, it outperforms the current development of Sb_2Se_3-based flexible photodetectors, and demonstrates a comparable performance to well-researched state-of-the-art flexible photodetectors.

2.2 Analysis of physical mechanisms

After the performance evaluations mentioned above, it is surprising to discover that this flexible Sb_2Se_3 photodetector has achieved comparable performance in aspects such as responsivity and response speed when compared to its rigid counterpart prepared by the same process (Fig. S6 in the ESM). In order to further validate its physical mechanism, the microstructure, defects and interface characteristics were systematically investigated. Figures 3(a) and 3(b) display the surface SEM images of the as-prepared Sb_2Se_3 thin films grown on rigid glass and flexible PI substrates, respectively.

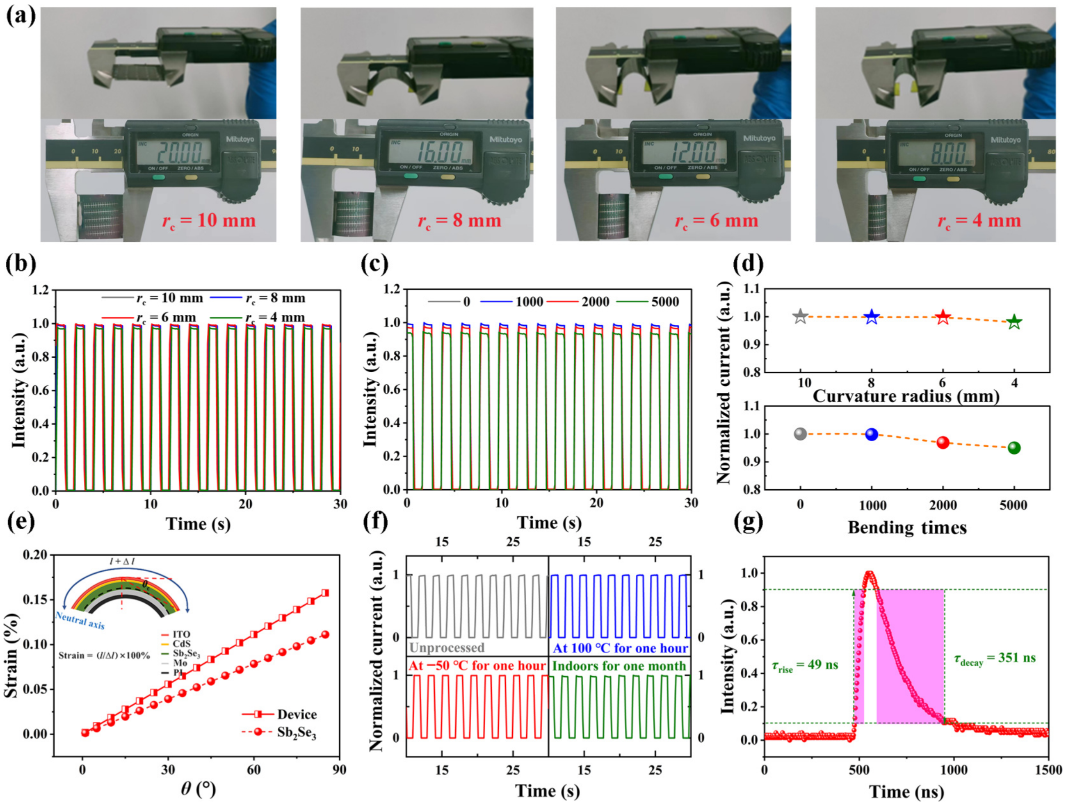

Figure 2 Flexibility characteristics of the Sb_2Se_3 thin-film photodetector. (a) Photographs of the flexible photodetector under 10, 8, 6, and 4 mm bending curvature radius. (b) Temporal photocurrent response of the flexible photodetector under different bending curvature radius. (c) Temporal photocurrent response of the flexible device with different bending cycles. (d) Normalized current as a function of bending curvature radius and bending cycles. (e) The strain of the whole device and Sb_2Se_3 layer under different bending curvature. (f) The stability of the flexible device in various simulated working environments. (g) Transient photo-response of the flexible device under a pulsed laser irradiation (pulse width of 3 ns).

Table 1 Comparison of key performance parameters between this work and some previously reported flexible photodetectors

Photodetectors	R (A·W^{-1})	D^* (Jones)	τ_{rise}/τ_{decay}	NEP (W)	LDR (dB)	Year	Ref.
Sb_2Se_3/CdS	0.51@635 nm	1.32×10^{13} [a]	49/351 ns	2.53×10^{-14}	109	2024	This work
Sb_2Se_3/CdS	0.42@625 nm	2.4×10^{11} [a]	1.8/1.6 μs	2.3×10^{-12}	95	2020	Chen [13]
Sb_2Se_3/ZnO	0.0078@905 nm	2.45×10^{11} [a]	39/144 μs	—	—	2021	Jiang [31]
Sb_2Se_3/CdS	0.74@940 nm	5.1×10^{13} [b]	160/150 μs	—	102	2023	Wen [19]
Si/Ag	0.11@808 nm	5.5×10^{12} [b]	29/51 μs	—	—	2021	Zhang [32]
PbS CQDs/ZnO	0.38@620 nm	1.01×10^{12} [b]	4.8/5.1 μs	1.87×10^{-13}	85	2023	Liu [33]
Graphene/γ-InSe	0.468@360 nm	1.9×10^{12} [a]	45/66 ms	—	—	2024	Li [34]
$MoTe_2$/InSe	0.434@450 nm	1.65×10^{12} [b]	99/117 μs	—	—	2024	He [35]
SnO_2/$FASnI_3$	0.37@785 nm	2.2×10^{13} [a]	2.62/5.91 μs	2.1×10^{-13}	—	2024	Liu [29]
PEIE/P_3HT:ICBA	0.1@525 nm	1.1×10^{12} [a]	35/35 μs	1.12×10^{-12}	~ 160	2020	Canek [24]
PEDOT:PSS/ITO	0.53@830 nm	2.0×10^{12} [a]	91/102 ns	4×10^{-11}	130	2023	Zhu [36]

[a]The total noise determined realistic detectivity, i.e., $D^* = \frac{\sqrt{S\Delta f}}{\mathrm{NEP}}$. [b]The shot noise determined specific detectivity, i.e., $D^* = \frac{R}{\left(\frac{2qI_{\mathrm{dark}}}{S}\right)^{1/2}}$.

Both thin films demonstrate similarly compact and crack-free morphologies, accompanied with micro-sized grains, indicating highly compatible thermal expansion coefficients between PI substrate and Mo/Sb_2Se_3 layers. In addition, X-ray diffraction (XRD) patterns demonstrate that the flexible Sb_2Se_3 thin film also exhibits preferential [*hk*1] grown orientation, i.e., distinct diffraction peaks of (211), (221), and (002), as well as the absence of impurity signal as compared to that of rigid thin film (Fig. 3(c)). Raman spectra of the Sb_2Se_3 thin films exhibit two major peaks appearing at 191 and 212 cm^{-1}, matching well with the high-quality orthorhombic phase of Sb_2Se_3, and can be assigned to the Sb–Se vibrations in the Sb_2Se_3 pyramidal unit (Fig. S7 in the ESM). With no obvious substrate induced modification of film microstructure, the inherent characters of Sb_2Se_3 bulk defects and defects-assisted carrier recombination mechanism were further analyzed (Note S3 in the ESM). Temperature-dependent admittance spectra (*C*–*f*–*T*)

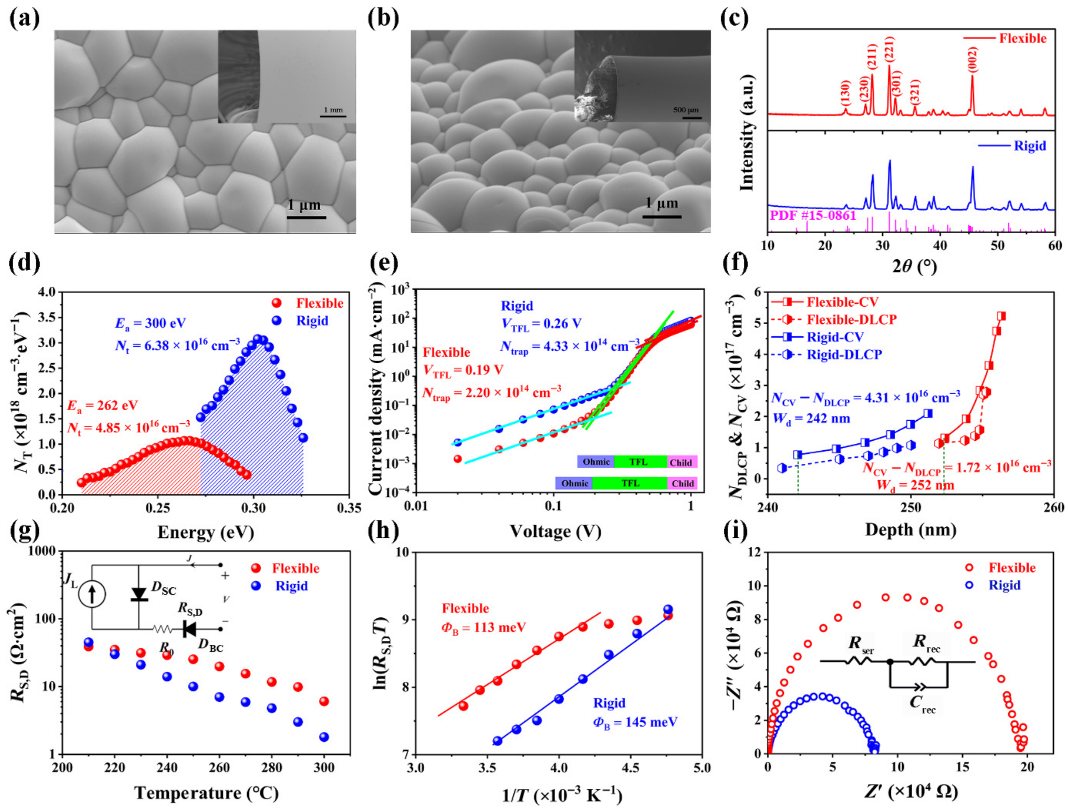

Figure 3 Comparison of the microstructure, defects and interface characteristics between rigid and flexible Sb_2Se_3 photodetectors. (a) and (b) Surface SEM images of rigid (a) and flexible (b) Sb_2Se_3 thin films. (c) XRD patterns of the rigid and flexible Sb_2Se_3 thin films. (d) Bulk defect distributions of the representative flexible and rigid Sb_2Se_3 thin-film photodetectors derived from the admittance spectra. (e) Logarithmic J–V curves, each curve includes Ohmic, TFL, and Child regions. (f) C–V and DLCP profiles. (g) Temperature dependence of dark series resistance $R_{S,D}$, along with a circuit model schematic diagram belonging to the Sb_2Se_3 photodetector (inset). (h) $\ln(R_{S,D}T)$ vs. $1/T$ plot for back contact barrier height determination. (i) Nyquist plots, and an equivalent circuit diagram (inset).

of the flexible and rigid Sb_2Se_3 thin-film photodetectors are shown in Fig. S8 in the ESM, and the corresponding Arrhenius plots with transition frequencies that associated to the rate of carrier trapping and emission from Sb_2Se_3 bulk defects are shown in Fig. S9 in the ESM. Accordingly, the activation energy E_a (i.e., the energy depth of the defect energy relative to the valence energy of p-type Sb_2Se_3) of the flexible sample is reduced from 300 to 262 meV as compared to rigid counterpart, under a reasonable Meyer–Nedel rule. Considering the Sb_2Se_3 associated intrinsic defect information from first-principle calculation results, the defects with a lower E_a of 262 meV can be assigned to V_{Se} vacancy defects, whereas defects with E_a of 300 meV are mainly Sb_{Se} antisite defects [39]. Furthermore, as shown in Fig. 3(d), the Gaussian distribution fitted defect states density N_T exhibits an important decline from 6.38×10^{16} (for rigid) to 4.85×10^{16} cm^{-3} (for flexible), signifying the passivation of Sb_2Se_3 bulk defects and non-radiative recombination, accounting for the device performance improvement. To gain deeper insights into the trap defect states, the dark logarithmic current density–voltage (J–V) curves of those two devices were analyzed under a typical space charge limited current (SCLC) concept (Fig. 3(e)) [17]. In general, this curve includes three distinct regions: the ohmic region covering low voltage areas, the trap-filled limit (TFL) region occupying intermediate voltage areas, and the trap-free Child region at high voltages. Notably, as the voltage crosses the kink point within the TFL region, there is a dramatic rise in current, suggesting that the injected carriers have effectively filled the trap states. Consequently, the onset voltages (V_{TFL}) for rigid and flexible devices are examined to be 0.26 and 0.19 V, correspondingly. Furthermore, the density of trap states (N_{trap}) was examined using the following equation [39]:

$$N_{trap} = \frac{2\varepsilon_0 \varepsilon_r V_{TEL}}{qL^2} \tag{8}$$

where L is the thickness of Sb_2Se_3 light absorber layer, ε_0 and ε_r are vacuum permittivity and relative permittivity, respectively. The obtained N_{trap} values exhibit a transitioning from 4.33×10^{14} to 2.20×10^{14} cm^{-3}, serving as a confirmation that the flexible device can not only compete with but potentially surpass the performance of its rigid counterpart. The heterojunction-dependent electrical properties have also been in-depth investigated based on a single exponential diode model (Note S4 in the ESM). The calculated reverse saturation current density (J_0 of 7.30×10^{-3} mA·cm^{-2}), series resistance (R_s of 4.11 Ω·cm^2) and diode ideality factor (A of 1.70) also confirms limited space charge region and/or interface non-radiative recombination inside the flexible device (Fig. S10 in the ESM). The $1/C^2$–V curves through capacitance–voltage (C–V) measurements authenticate a superior junction quality with essential built-in voltage (i.e., V_{bi} of 634 mV) to automatically separate the photo-generated electron–hole pairs in flexible device, as illustrated in Fig. S11 in the ESM. To clarify the correlation between interface defects and device responsivity and response speed, drive-level capacitance profiling (DLCP) measurements have been implemented since it is less sensitive to interface defects. The curves detailing C–V derived doping density (N_{CV}) and DLCP measured doping density (N_{DLCP}) as functions of the profile depth (x) can be elegantly characterized by [40]:

$$\begin{cases} N_{\mathrm{CV}} = \dfrac{-2\varepsilon_{\mathrm{r,n}} N_D}{\left(\dfrac{\mathrm{d}(1/c^2)}{\mathrm{d}V}\right) qS^2\varepsilon_0\varepsilon_{\mathrm{r,n}}\varepsilon_{\mathrm{r,p}}N_D + 2\varepsilon_{\mathrm{r,p}}} \\ N_{\mathrm{DLCP}} = -\dfrac{C_0^{\ 3}}{2q\varepsilon_0\varepsilon_{\mathrm{r,p}}S^2C_1} \\ x = \dfrac{\varepsilon_0\varepsilon_{\mathrm{r,p}}S}{C_0} \end{cases} \tag{9}$$

where $\varepsilon_{r,n}$ and $\varepsilon_{r,p}$ represent the relative permittivity of CdS and Sb_2Se_3, respectively, C_0 and C_1 are two quadratic fitting parameters derived from C–V curves. Specifically, the doping density N_{CV} includes the responses from free carriers, bulk defects, and interface defects, while N_{DLCP} offers a more accurate assessment of bulk defects and free carriers, thus the discrepancy between N_{CV} and N_{DLCP} corresponds to the interface defect density (N_i). Therefore, the obtained N_i value of 1.72×10^{16} cm^{-3} for flexible device is nearly half of 4.31×10^{16} cm^{-3} for rigid device (Fig. 3(f)). The lower interfacial defects can suppress the carrier recombination at the interface, contributing to its superior responsivity. Furthermore, the flexible device unveils a superior depletion width (W_d of 252 nm), which can also accelerate the minority carrier transport, performing a crucial role to elevate the device response speed. We then shift our focus to the back contact interface, exploring the temperature-dependent dark series resistance ($R_{S,D}$) and back contact barrier (Φ_B) especially under key substrate modification. To be specific, $R_{S,D}$ values and Φ_B values can be determined by the following equations [41]:

$$\begin{cases} \dfrac{\mathrm{d}V}{\mathrm{d}J} = R_{\mathrm{S,D}} + \dfrac{AKT}{q(J - G_{\mathrm{S,D}}V)} \\ R_{\mathrm{S,D}} = R_0 + \dfrac{k}{qA^*T} \times \exp\left(\dfrac{\Phi_{\mathrm{B}}}{kT}\right) \end{cases} \tag{10}$$

where $G_{S,D}$ signifies the dark shunt conductance, and it is more credible without light-induced variations, k and A^* are Boltzmann constant and Richardson constant, respectively, R_0 is the background series resistance and is expected to be insignificant at temperature $T < 300$ K. As illustrated in Fig. 3(g), the $R_{S,D}$ values of rigid Sb_2Se_3 photodetector significantly increase with decreasing temperature, while it tends to a slower evolution and even a saturated state for the flexible device, indicating a mitigatory blocking effect at PI/Mo/Sb_2Se_3 back contact interface, thereby enhancing the charge carrier transport. A typical Schottky diode circuit model can also be used to understand this mechanism (inset in Fig. 3(g), where R_0 is background series resistance, D_{BC} is back contact diode, D_{SC} is primary solar cell diode and J_L is light current density). The exact Φ_B values are then obtained by fitting the corresponding linear region of $\ln(R_{S,D}T)$ versus $1/T$ plots (Fig. 3(h)). The extracted Φ_B values of the rigid and flexible devices are 145 and 113 meV, respectively. A smaller Φ_B indicates a better Ohmic contact, strengthening an accelerated carrier extraction and transport at the buried back contact interface for flexible Sb_2Se_3 photodetector. Finally, the kinetics of carrier transfer and recombination were examined in more detail through electrochemical impedance spectroscopy (EIS) [42, 43]. A comparison of the Nyquist plots for rigid and flexible devices, as well as a schematic of an equivalent circuit are provided in Fig. 3(i). Specifically, R_{ser}, R_{rec}, and C_{rec} stand for series resistance, recombination resistance, and recombination capacitance, respectively. R_{ser} equals to the x-axis intercept (Z'), thus, the yield R_{ser} values for rigid and flexible scenarios are 8×10^4 and 1.9×10^5 Ω·cm^2, respectively, echoing the carrier transport ability evolution. R_{rec} are directly correlated with the arc's diameter length, it reflects that the flexible device possesses a clearly lowered likelihood of charge recombination. Importantly, higher R_{rec} also encourages a noteworthy reduction in the thermal noise (defined as $\sqrt{4kT\Delta f/R_{rec}}$), further accounting for its higher detectivity [28]. The aforementioned traits connected to defects, bulk and interface properties are summarized in Table 2, these key elements help to improve the generation, separation and transfer of charge carriers, thus improve the responsivity, detectivity and response speed of the flexible Sb_2Se_3 photodetector.

2.3 Color imaging application demonstration

Since this flexible Sb_2Se_3 photodetector possesses superior performance, an innovative exploration of its potential applications was conducted. Firstly, an imaging system was engineered to investigate its imaging capability, which employed a single-pixel scanning technique and encompassed essential components, i.e., flexible Sb_2Se_3 photodetector array, a 450 and a 905 nm laser, a mask bearing a "CF" pattern, Keithley 2400 source meters and computational unit, as depicted in Fig. 4(a). Interestingly, a Vis/NIR image of remarkable clarity emerged sans any external power supply, accomplished by adeptly converting the yield signal in the form of current to a "gray code" representation (as delineated in Fig. 4(d)). However, for the original Vis/NIR image, the gray value ratio is approximately 1:1, rendering it effectively indistinguishable. Noteworthy is the phenomenon observed when subjecting the photodetector to bias conditions. To be specific, at −1 V bias, the image exhibited heightened luminosity but retained its intrinsic nature (Fig. 4(e)). Yet, when a +1 V bias was applied, the NIR image (i.e., corresponds to letter F) nearly vanished, while the Vis image experienced an unanticipated surge in luminosity (Fig. 4(f)). This discerning feature emphasizes the effortless transition from dual-color imaging to single-color imaging, attainable with the mere application of a modest bias. The energy band dynamics might play important role in this evolution, thus, the energy level information of Sb_2Se_3 and CdS thin films were first analyzed by using ultraviolet photoelectron spectroscopy (UPS, Note S5 and Fig. S12 in the ESM). Subsequently, as shown in Fig. 4(g), the as-constructed Sb_2Se_3/CdS heterojunction reveals an ideal energy band bending with a conduction band offset (CBO) of 0.26 eV, indicative of a "spike-like" band alignment [17]. This benign alignment might prevent carriers with accumulation in the vicinity of the heterointerface, and expedite the separation and conveyance of charge carriers. Under the influence of reverse bias voltage, the heterojunction-dependent built-in field aligns concordantly with the applied field. The energy band of CdS gracefully descends in relation to Sb_2Se_3 (Fig. 4(h)), a maneuver that amplifies the

Table 2 Summary of heterojunction and interface derived device parameters

Devices	E_a (meV)	N_t (cm^{-3})	V_{TFL} (V)	N_{trap} (cm^{-3})	W_d (nm)	N_i (cm^{-3})	Φ_B (meV)	R_{ser} (Ω)
Rigid	300	6.38×10^{16}	0.26	4.33×10^{14}	242	4.31×10^{16}	145	8×10^4
Flexible	262	4.85×10^{16}	0.19	2.20×10^{14}	252	1.72×10^{16}	113	1.9×10^5

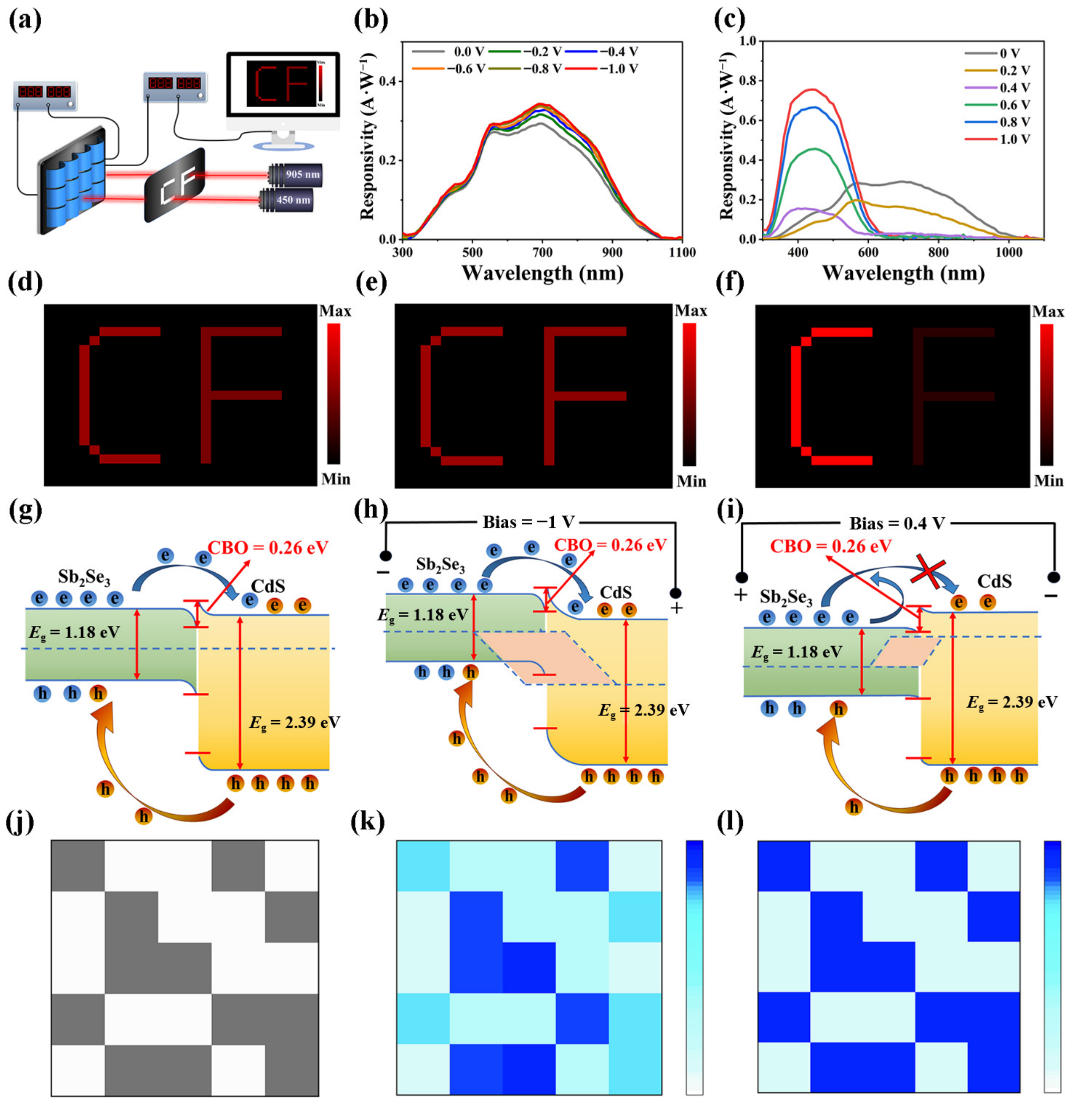

Figure 4 Color imaging application demonstration. (a) Schematic illustration of the measurement setup for light imaging applications. The wavelength-dependent responsivity curves for the flexible Sb_2Se_3 photodetector under illumination: (b) at reverse bias, and (c) at forward bias. (d) Dual-color (left: visible (450 nm), and right: NIR (905 nm)) imaging results through the imaging system at bias voltage of 0 V. (e) The imaging result obtained at a bias voltage of −1 V. (f) The imaging result obtained at a bias voltage of 1 V. The schematic energy band diagrams for Sb_2Se_3/CdS heterojunction at 0 V (g), −1 V (h), and 0.4 V (i). (j) The original QR code. (k) The imaging result of the QR code under bent state by applying rigid Sb_2Se_3 photodetector as the detector and at a bias voltage of 1 V. (l) The imaging result of the QR code under bent state by applying flexible Sb_2Se_3 photodetector as the detector and at 1 V.

efficiency of charge carrier extraction within the heterojunction. Thus, in turn, culminates in the progressive enhancement of the device responsivity with increasing negative bias voltage (as illustrated in Fig. 4(b)). Conversely, when subjected to a forward bias, the applied field contends with the inherent field's direction [44]. In this scenario, energy band of CdS ascends relative to Sb_2Se_3, a shift that curtails the populace of free charge carriers and their effective extraction within the heterojunction (Fig. 4(i)). The efficiency of exciton dissociation (i.e., free charge carrier generation) and separation typically decreases with weakening of the electric field intensity. Thus, when forward bias escalates, the device responsivity within the 600–1050 nm range undergoes a gradual reduction, especially a pronounced diminishment in the face of dwindling electric field intensity over the inherent CBO (Fig. 4(c)). Moreover, when the external bias voltage is greater than 0.4 V (a threshold value), the built-in electric field generated by Sb_2Se_3 has been cancelled, the carrier movement is driven by the external voltage, leading to the change of current direction. The steady boost in responsivity perceived within the 300–600 nm wavelength range can be credited to a transition from a self-driven detector to a photoconductive detector, which is a significant phenomenon that contributes to photo-response tailoring. Drawing inspiration from this fundamental principle, we devised a quick response (QR) code pattern seamlessly integrated with a detector imaging system (depicted in Fig. 4(j)). Under the irradiation of a 450 nm laser, the imaging outcomes of the curved QR code pattern are detailed in Fig. S13 in the ESM. The resolution suffers due to the minimal photocurrent response and the reduced mapping area resulting from the curvature of the QR code pattern. In a quest to heighten the pattern resolution, the applied bias voltage was elevated to +1 V, yielding the results showcased in Fig. 4(k). Evidently, there is a substantial enhancement in resolution compared to 0 V bias outcome, allowing for a more distinct identification of the QR code. However, challenges persist when confronted with intricacies inherent in more complex patterns. In a culminating step, the substitution of the rigid apparatus with a flexible Sb_2Se_3 photodetector is illustrated in Fig. 4(l). Notably, the achieved resolution is exceptionally high, which can be attributed to the innate adaptability of the flexible detector to the curvature of the pattern, with the mapped laser area experiencing minimal alteration, resulting in near-constant generated current.

2.4 Physiological monitoring application demonstration

Photoplethysmography (PPG) is an optoelectronic technique that can detect changes in blood volume within the tissue vascular bed, which is extensively utilized for physiological monitoring in applications such as vascular diagnostics and pulse oximetry [45–47]. Heart rate (HR) and arterial blood oxygen saturation (SaO_2) can be non-invasively assessed using pulse oximetry, which is made possible by PPG readings. These measures are essential for both clinical and mobile patient monitoring. Owing to their significant differences in absorption coefficients between oxyhemoglobin (HbO_2) and deoxyhemoglobin (Hb), red and NIR LEDs are commonly chosen as light sources in pulse oximetry sensor systems. Notably, our flexible Sb_2Se_3 photodetector exhibits high responsivity in the red and NIR wavelength regions, making it well-suited for SaO_2 measurements. Herein, data collection and computation are performed using a self-constructed pulse oximetry system comprised of a 635 and a 905 nm laser, a highly precise Keithley 2400 source meter, and the flexible Sb_2Se_3 photodetector (Fig. 5(a)). As depicted in Fig. 5(b), a microcontroller circuit with a power supply and laser emits red (635 nm) light, which penetrates the finger, where it is partially absorbed by the microvascular bed of the skin, with the remainder being reflected by other tissues. The light that passes through the tissue is then captured by the flexible photodetector on the contrary side, and converting this optical signal into electrical signal through photoelectric effect. The ongoing changes in arterial blood volume at the sensing area cause light absorption within the finger to fluctuate continuously during the systole and diastole phases, ranging electrical currents from peak values to minimum values. These variations can be converted into a pulse signal, which is analogous to the heartbeat of a person. The resulting PPG signals and HR information obtained from both the red and NIR light using commercial rigid Si photodetector and flexible Sb_2Se_3 photodetector are presented in Figs. 5(c) and 5(d), respectively. The ratio of absorbed light (R_{os}) and SaO_2 values were calculated using the following equations [48–50]:

$$\begin{cases} R_{os} = \dfrac{\ln(T_{rd})}{\ln(T_{ir})} \\ SaO_2(R_{os}) = \dfrac{\varepsilon_{rd,Hb} - \varepsilon_{ir,Hb} R_{os}}{(\varepsilon_{rd,Hb} - \varepsilon_{rd,HbO_2}) + (\varepsilon_{ir,HbO_2} - \varepsilon_{ir,Hb}) R_{os}} \end{cases} \quad (11)$$

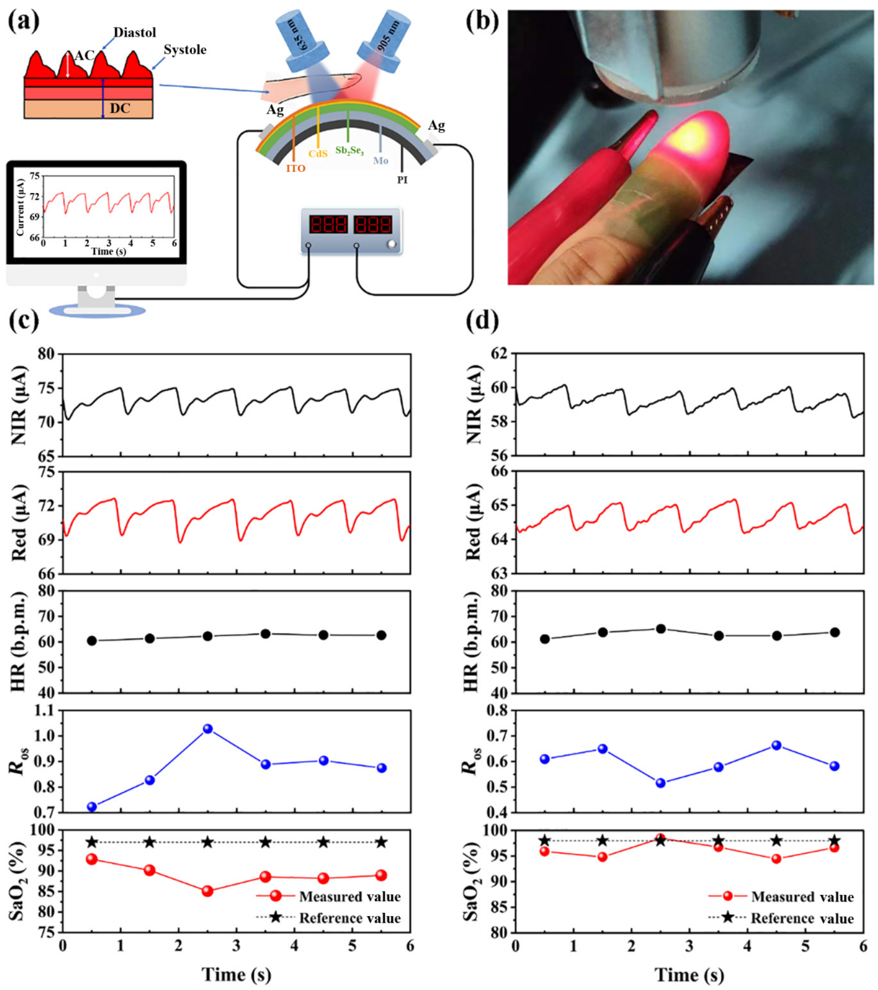

Figure 5 Physiological monitoring application demonstration. (a) Schematic circuit diagram of the PPG monitoring system. (b) A representative red laser was placed above the finger and the transmitted light was collected with a flexible Sb_2Se_3 photodetector below the finger. Under NIR and red laser light irradiation, simultaneous HR and arterial SaO_2 monitoring based on a commercially rigid Si photodetector (c), and the flexible Sb_2Se_3 thin-film photodetector (d).

where T_{rd} is the transmittance of red light, T_{ir} is the transmittance of NIR light, ε_{Hb} and ε_{HbO_2} are the molar absorption coefficients of Hb and HbO_2, respectively. According to the commercial Si photodetector, the obtained human HR value is approximately 62 beats per minute, consistent with the standard value, however, SaO_2 values range from 85% to 92%, exhibiting some noticeable deviations when compared to the readings from the commercial fingertip oximeter (with SaO_2 at 97%–98%, Fig. S14 in the ESM). In comparison, the HR and SaO_2 values produced by our flexible Sb_2Se_3 photodetector are 60–65 beats per minute and 96%–100%, respectively. Both values closely match the results from the commercial fingertip oximeter. Importantly, the measurement variance of SaO_2 exhibits an obvious decrease from 23‰ for Si photodetector to 13‰ for Sb_2Se_3 photodetector. Actually, this discrepancy can be attributed to the commercial Si detector's imperfect fit to the finger and the presence of greater noise interference. In contrast, the flexible Sb_2Se_3 thin-film photodetector conforms seamlessly to the finger, experiences less interference from external light sources, and thereby exhibits more stable and superior performance, demonstrating great application potential in wearable physiological detection and monitoring.

3 Conclusions

In summary, we developed a flexible prototype Sb_2Se_3 thin-film photodetector involving flexible PI substrate, Sb_2Se_3 light absorber layer and CdS buffer layer. The champion device demonstrated self-powered and broadband characters, outstanding R of 0.51 $A\cdot W^{-1}$, D^* up to 1.32×10^{13} Jones, NEP of 2.53×10^{-14} W, LDR of 109 dB, ultra-fast response speed with rise and decay times of 49/351 ns, as well as exceptionally excellent stability to stand significant bending curvature radius of 4 mm and bending cycles over 5000×. Such performance is closely related to the high-quality flexible Sb_2Se_3 film with large grains, preferential [*hk*1] growth orientation and suppressed bulk defects, as well as benign interfaces at both back contact interface (e.g., appropriate dark series resistance and back contact barrier) and heterojunction interface (e.g., large built-in voltage and low interface defects), presenting overall optimization of the charge carrier dynamics involving generation, separation and transport. Notably, this flexible photodetector demonstrated interesting imaging capability to convert dual-color images into single-color images and distinct QR code identification under bias voltage induced band alignment modulation. Furthermore, based on this flexible photodetector, we presented an accurate evaluation of both HR and SaO_2 for a person under PPG readings for the first time, surpassing the commercial rigid Si photodetectors in terms of precision and flexibility. This groundbreaking research is anticipated to set the foundation for the advancement of highly efficient flexible Sb_2Se_3 photodetectors for future commercialization.

4 Experimental section

4.1 Deposition of flexible Sb_2Se_3 thin film

The flexible PI was chosen as the substrate, and was sequentially cleaned by detergent, acetone, isopropanol, and deionized water. A Mo back contact layer was then attached on PI through direct-current (DC) magnetron sputtering. In subsequent, a controllable radio-frequency (RF) magnetron sputtering of the Sb precursor followed with post-selenization treatment was implemented to achieve the thermodynamic/kinetic growth of flexible and crystalline Sb_2Se_3 thin film. The detailed procedural setup closely followed the description provided in our earlier report involving Sb_2Se_3 preparation on rigid substrate [17], except a crucial selenization temperature of 400 °C.

4.2 Fabrication of flexible Sb_2Se_3 thin-film photodetector

After the preparation of flexible Sb_2Se_3 thin film, the n-type CdS buffer layer (approximately 80 nm) was deposited using a typical chemical bath deposition (CBD) method in accordance with the previously reported recipe [17]. An important Sb_2Se_3/CdS heterojunction interface heat treatment was also implemented in a 300 °C vacuum tube for 5 min. Following this, DC magnetron sputtering system was used to deposit an indium tin oxide (ITO) window layer, which was conducted by maintaining a steady gas flow at 30 sccm and 10 sccm for argon and oxygen under a constant power of 120 W and a pressure of 0.4 Pa. Finally, photovoltaic-type flexible thin-film photodetector with configuration of PI/Mo/Sb_2Se_3/CdS/ITO/Ag was constructed by thermally evaporated silver (Ag) grids as metallic contact.

4.3 Characterizations

An X-ray diffractometer (XRD), specifically an Ultima-iv model, equipped with CuKα radiation, was employed to analyze the crystal information of the Sb_2Se_3 absorber layer. To observe the cross-sectional and surface morphologies, a thermal field emission scanning electron microscope (SEM) was utilized, with a Zeiss SUPRA 55 model being the instrument choice. Transmission electron microscopy (TEM) characterization was performed on the FEI Titan cube Themis G2 300 microscope. Raman spectra were collected using a RenishawinVia spectrometer under an excitation wavelength of 532 nm. Further investigation into the energy-level information was carried out through ultraviolet photoelectron spectroscopy (UPS). A 635 nm power-adjustable laser (MRL-III-635L-80 mW) and a 905 nm laser (MDL-III-905-100 mW) with source meters (Keithley 2400) were employed to test the photodetection performance of the Sb_2Se_3 thin-film photodetectors. These measurements were conducted within a shielded enclosure. Dynamic photo-response measurements were conducted using either a pulsed laser with a pulse width of 3 ns or a modulated laser driven by a signal generator (UTG2025A). The recorded signals were captured by a high-speed oscilloscope (DSOX1202A). The wavelength-dependent responsivity was determined using a Zolix SCS101 system, featuring a monochromator and a source meter. *C*–*V* measurements were conducted with an amplitude of 30 mV and a frequency of 10 kHz, while drive-level capacitance profiling (DLCP) measurements involved an AC amplitude ranging from 20 to 140 mV and a DC bias voltage ranging from −0.2 to 0.2 V, both in dark condition. The temperature-dependent dark series resistance and back contact barrier analysis were performed using a Keithley 4200A-SCS system and a Lakeshore 325 temperature controller. EIS data were acquired through a CHI660e electrochemical workstation. In imaging measurements, 450 and 905 nm laser light, and Keithley 2400 source meters were employed to collect the current magnitude. In the photoplethysmography (PPG) demonstration system, a flexible Sb_2Se_3 photodetector was utilized as the receiver, 635 and 905 nm laser light were introduced. A portion of the incident light emitted from the laser passed through the tissue and was subsequently captured by the photodetector. The resulting output electrical signals were recorded and monitored using CHI660e electrochemical workstation.

Electronic Supplementary Material: Supplementary material (Fig. S1: HAADF-STEM image viewed at Sb_2Se_3 absorber layer region; Fig. S2: Semi-logarithmic *I*–*V* curves of the flexible Sb_2Se_3

photodetector; Note S1 and Fig. S3: Electronic noise measurements; Fig. S4: Incident laser (905 nm) light power-dependent device responsivity and specific detectivity; Fig. S5: Noise power spectra of the flexible Sb_2Se_3 photodetector; Fig. S6: Comparison of the response time and responsivity of the flexible and rigid Sb_2Se_3 photodetectors; Fig. S7: Raman spectra of the Sb_2Se_3 thin films deposited on flexible and rigid substrates; Note S2: Strain analysis; Note S3: Admittance spectroscopy analysis; Fig. S8: Capacitance–frequency–temperature (*C*–*f*–*T*) spectra of the flexible and rigid Sb_2Se_3 photodetectors; Fig. S9: Defect activation energies E_a of the devices; Note S4: Analysis of single-exponential diode characters; Fig. S10: Reverse saturation current density J_0 and shunt conductance *G* characterizations; Fig. S11: $1/C^2$–V plots; Note S5: Energy band information of the CdS and Sb_2Se_3 thin films; Fig. S12: UPS characterizations; Fig. S13: The imaging result of the QR code by applying rigid Sb_2Se_3 photodetector; Fig. S14: The standard heart rate and arterial blood oxygen saturation values obtained from a commercial oximeter (medisana)) is available in the online version of this article at https://doi.org/10.26599/NR.2025.94907159.

Data availability

All data needed to support the conclusions in the paper are presented in the manuscript and the ESM. Additional data related to this paper may be requested from the corresponding author upon request.

Acknowledgements

This work was supported by the National Natural Science Foundation of China (Nos. 62104156, 62074102, 22275180, and 2019YFA0405600), Guangdong Basic and Applied Basic Research Foundation (Nos. 2023A1515011256 and 2022A1515010979) China, and Shenzhen Science and Technology Program (No. GJHZ20240218113809019).

Declaration of competing interest

All the contributing authors report no conflict of interests in this work.

Author contribution statement

S. C.: Conceptualization, funding acquisition, investigation, methodology, writing – original draft. H.-B. L.: Data curation, investigation. Y. F.: Data curation, investigation. G.-Q. L.: Investigation, methodology. M. I.: Writing – review & editing. J. L. Investigation. J.-M. L.: Investigation, methodology. B. C.: Writing – review & editing. J.-T. L.: Visualization, writing – review & editing. L. M. D.: Supervision, validation, visualization, writing – review & editing. T. C.: Supervision, validation, visualization, writing – review & editing. G.-X. L.: Conceptualization, funding acquisition, supervision, writing – review & editing.

Use of AI statement

None

References

[1] Huang, M. Q.; Wang, M. L.; Chen, C.; Ma, Z. W.; Li, X. F.; Han, J. B.; Wu, Y. Q. Broadband black-phosphorus photodetectors with high responsivity. *Adv. Mater.* **2016**, *28*, 3481–3485.

[2] Shen, Y. C.; Lee, C. Y.; Wang, H. H.; Kao, M. H.; Hou, P. C.; Chen, Y. Y.; Huang, W. H.; Shen, C. H.; Chueh, Y. L. Embedded integration of Sb_2Se_3 film by low-temperature plasma-assisted chemical vapor reaction with polycrystalline Si transistor for high-performance flexible visible-to-near-infrared photodetector. *ACS Nano* **2023**, *17*, 2019–2028.

[3] Wu, Q. C.; Qian, J.; Wang, Y. C.; Xing, L. W.; Wei, Z. Y.; Gao, X.; Li, Y. R.; Liu, Z. F.; Liu, H. T.; Shu, H. W. et al. Waveguide-integrated twisted bilayer graphene photodetectors. *Nat. Commun.* **2024**, *15*, 3688.

[4] Chai, Y. Silicon photodiodes that multiply. *Nat. Electron.* **2022**, *5*, 483–484.

[5] Chen, K.; Deng, C. C.; Zou, C.; Zhao, Z. X.; Liu, Q.; Wang, X. F.; He, L. F.; Gao, F. L.; Zhao, W.; Li, S. T. Plasmonic hot-hole injection combined with patterned substrate for performance improvement in trapezoidal PIN GaN microwire self-powered ultraviolet photodetector. *Nano Energy* **2022**, *104*, 107926.

[6] Wang, J. L.; Li, S. P.; Wang, T. T.; Guan, F.; Zhao, L. J.; Li, L. H.; Zhang, J. H.; Qiao, G. J. Solution-processed Sb_2Se_3 on TiO_2 thin films toward oxidation- and moisture-resistant, self-powered photodetectors. *ACS Appl. Mater. Interfaces* **2020**, *12*, 38341–38349.

[7] Wang, L.; Li, D. B.; Li, K. H.; Chen, C.; Deng, H. X.; Gao, L.; Zhao, Y.; Jiang, F.; Li, L. Y.; Huang, F. et al. Stable 6%-efficient Sb_2Se_3 solar cells with a ZnO buffer layer. *Nat. Energy* **2017**, *2*, 17046.

[8] Zhou, Y.; Wang, L.; Chen, S. Y.; Qin, S. K.; Liu, X. S.; Chen, J.; Xue, D. J.; Luo, M.; Cao, Y. Z.; Cheng, Y. B. et al. Thin-film Sb_2Se_3 photovoltaics with oriented one-dimensional ribbons and benign grain boundaries. *Nat. Photon.* **2015**, *9*, 409–415.

[9] Zhai, T. Y.; Ye, M. F.; Li, L.; Fang, X. S.; Liao, M. Y.; Li, Y. F.; Koide, Y.; Bando, Y.; Golberg, D. Single-crystalline Sb_2Se_3 nanowires for high-performance field emitters and photodetectors. *Adv. Mater.* **2010**, *22*, 4530–4533.

[10] Tang, R.; Chen, S.; Zheng, Z. H.; Su, Z. H.; Luo, J. T.; Fan, P.; Zhang, X. H.; Tang, J.; Liang, G. X. Heterojunction annealing enabling record open-circuit voltage in antimony triselenide solar cells. *Adv. Mater.* **2022**, *34*, 2109078.

[11] Liang, G. X.; Chen, M. D.; Ishaq, M.; Li, X. R.; Tang, R.; Zheng, Z. H.; Su, Z. H.; Fan, P.; Zhang, X. H.; Chen, S. Crystal growth promotion and defects healing enable minimum open-circuit voltage deficit in antimony selenide solar cells. *Adv. Sci.* **2022**, *9*, 2105142.

[12] Fan, P.; Chen, G. J.; Chen, S.; Zheng, Z. H.; Azam, M.; Ahmad, N.; Su, Z. H.; Liang, G. X.; Zhang, X. H.; Chen, Z. G. Quasi-vertically oriented Sb_2Se_3 thin-film solar cells with open-circuit voltage exceeding 500 mV prepared via close-space sublimation and selenization. *ACS Appl. Mater. Interfaces* **2021**, *13*, 46671–46680.

[13] Zhang, S.; Wang, H.; Kirchner, M. M.; Liu, J.; Luo, H.; Ren, Y.; Yuan, C.; Hattori, H. T.; Miroshnichenko, A. E.; Lei, W. Ultrathin Sb_2Se_3 nanowires for polarimetric imaging photodetectors with a high signal/noise ratio. *Adv. Mater. Interfaces* **2022**, *9*, 2200448.

[14] Chen, C.; Li, K. H.; Li, F.; Wu, B. Z.; Jiang, P. F.; Wu, H. D.; Lu, S. C.; Tu, G. L.; Liu, Z.; Tang, J. One-dimensional Sb_2Se_3 enabling a highly flexible photodiode for light-source-free heart rate detection. *ACS Photonics* **2020**, *7*, 352–360.

[15] Chen, S.; Qiao, X. S.; Wang, F. X.; Luo, Q.; Zhang, X. H.; Wan, X.; Xu, Y.; Fan, X. P. Facile synthesis of hybrid nanorods with the $Sb_2Se_3/AgSbSe_2$ heterojunction structure for high performance photodetectors. *Nanoscale* **2016**, *8*, 2277–2283.

[16] Li, G.; Li, Z. Q.; Chen, J. W.; Chen, X.; Qiao, S.; Wang, S. F.; Xu, Y.; Mai, Y. Self-powered, high-speed Sb_2Se_3/Si heterojunction photodetector with close spaced sublimation processed Sb_2Se_3 layer. *J. Alloys Compd.* **2018**, *737*, 67–73.

[17] Chen, S.; Fu, Y.; Ishaq, M.; Li, C. H.; Ren, D. L.; Su, Z. H.; Qiao, X.; Fan, P.; Liang, G. X.; Tang, J. Carrier recombination suppression and transport enhancement enable high-performance self-powered broadband Sb_2Se_3 photodetectors. *InfoMat* **2023**, *5*, e12400.

[18] Liang, Y.; Wang, Y. Y.; Wang, J. N.; Wu, S. M.; Jiang, D. Y.; Lian, J. B. High-performance flexible photodetectors based on single-crystalline Sb_2Se_3 nanowires. *RSC Adv.* **2016**, *6*, 11501–11506.

[19] Chen, G. H.; Wang, W. L.; Wang, C. D.; Ding, T.; Yang, Q. Controlled synthesis of ultrathin Sb_2Se_3 nanowires and application for flexible photodetectors. *Adv. Sci.* **2015**, *2*, 1500109.

[20] Wen, X. X.; Lu, Z. H.; Li, B. X.; Wang, G. C.; Washington, M. A.; Zhao, Q.; Lu, T. M. Free-standing [001]-oriented one-dimensional crystal-structured antimony selenide films for self-powered flexible near-infrared photodetectors. *Chem. Eng. J.* **2023**, *462*, 142026.

[21] Wu, C.; Luo, X. Z.; Yu, X. M.; Yu, X.; Lin, K.; Li, M. H.; Li, Z. H.; Cao, Y.; Zhou, Y. T. Improving performance of ZnO Schottky photodetector by inserting MXenes modified-layer. *Chin. Chem. Lett.* **2023**, *34*, 107881.

[22] Zhu, X. F.; Duan, W. S.; Meng, X. C.; Jia, X. Y.; Zhang, Y. H.; Zhou, P. Y.; Wang, M. J.; Zheng, H. X.; Fan, C. Visible-to-near-infrared photodetectors based on SnS/$SnSe_2$ and SnSe/$SnSe_2$ p-n heterostructures with a fast response speed and high normalized detectivity. *J. Semicond.* **2024**, *45*, 032703.

[23] Liu, J.; Liu, P. L.; Chen, D. Y.; Shi, T. L.; Qu, X. X.; Chen, L.; Wu, T.; Ke, J. P.; Xiong, K.; Li, M. Y. et al. A near-infrared colloidal quantum dot imager with monolithically integrated readout circuitry. *Nat. Electron.* **2022**, *5*, 443–451.

[24] Fang, Y. J.; Huang, J. S. Resolving weak light of Sub-picowatt per square centimeter by hybrid perovskite photodetectors enabled by noise reduction. *Adv. Mater.* **2015**, *27*, 2804–2810.

[25] Fuentes-Hernandez, C.; Chou, W. F.; Khan, T. M.; Diniz, L.; Lukens, J.; Larrain, F. A.; Rodriguez-Toro, V. A.; Kippelen, B. Large-area low-noise flexible organic photodiodes for detecting faint visible light. *Science* **2020**, *370*, 698–701.

[26] Fang, Y. J.; Armin, A.; Meredith, P.; Huang, J. S. Accurate characterization of next-generation thin-film photodetectors. *Nat. Photon.* **2019**, *13*, 1–4.

[27] Liang, G. X.; Li, C. H.; Zhao, J.; Fu, Y.; Yu, Z. X.; Zheng, Z. H.; Su, Z. H.; Fan, P.; Zhang, X. H.; Luo, J. T. et al. Self-powered broadband kesterite photodetector with ultrahigh specific detectivity for weak light applications. *SusMat* **2023**, *3*, 682–696.

[28] Wu, Z. H.; Yao, W. C.; London, A. E.; Azoulay, J. D.; Ng, T. N. Elucidating the detectivity limits in shortwave infrared organic photodiodes. *Adv. Funct. Mater.* **2018**, *28*, 1800391.

[29] Xin, Y.; Jiang, J. C.; Lu, Y. F.; Liang, H. W.; Zeng, Y. J.; Ye, Z. Z. Self-powered broad spectral photodetector with ultrahigh responsivity and fast response based on Sb_2Se_3/VO_2 heterojunction. *Adv. Mater. Interfaces* **2021**, *8*, 2100058.

[30] Wang, H.; Zhang, Z. K.; Luo, H. J.; Zhang, S. Q.; Pan, W. W.; Liu, J. L.; Ren, Y. L.; Lei, W. A case study of 2D Bi_2O_2Se nanoplate near-infrared photodetectors from the perspective of practical applications. *Adv. Opt. Mater.* **2024**, *12*, 2401404.

[31] Liu, T. H.; Wang, J. F.; Liu, Y. S.; Min, L. L.; Wang, L. X.; Yuan, Z. Q.; Sun, H. X.; Huang, L.; Li, L.; Meng, X. Y. Cyano-coordinated tin halide perovskites for wearable health monitoring and weak light imaging. *Adv. Mater.* **2024**, *36*, 2400090.

[32] Xin, H. Y.; Yang, S. Y.; Wang, Y.; Sulaman, M.; Zhang, Z. H.; Ge, Z. H.; Hu, J. M.; Wang, S. L.; Zou, B. S.; Tang, L. B. Self-driven broadband photodetectors on flexible silicon nanowires substrate by forming a heterojunction with reduced graphene oxide. *J. Mater. Chem. C* **2024**, *12*, 3105–3115.

[33] Jiang, J. C.; Guo, Y. J.; Weng, X. L.; Long, F. C.; Xin, Y.; Lu, Y. F.; Ye, Z. Z.; Ruan, S. C.; Zeng, Y. Z. A tailorable polarity-flipping response in self-powered, flexible Sb_2Se_3/ZnO bilayer photodetectors. *J. Mater. Chem. C* **2021**, *9*, 4978–4988.

[34] Zhang, B. C.; Shi, Y. H.; Mao, J.; Huang, S. Y.; Shao, Z. B.; Zheng, C. J.; Jie, J. S.; Zhang, X. H. Single-crystalline silicon frameworks: A new platform for transparent flexible optoelectronics. *Adv. Mater.* **2021**, *33*, 2008171.

[35] Liu, J.; Liu, P. L.; Shi, T. L.; Ke, M.; Xiong, K.; Liu, Y. X.; Chen, L.; Zhang, L. X.; Liang, X. Y.; Li, H. et al. Flexible and broadband colloidal quantum dots photodiode array for pixel-level X-ray to near-infrared image fusion. *Nat. Commun.* **2023**, *14*, 5352.

[36] Li, Y. Z.; Pan, J. Y.; Yan, C. X.; Li, J. X.; Xin, W.; Zhang, Y. T.; Liu, W. Z.; Liu, X. F.; Xu, H. Y.; Liu, Y. C. Efficient carrier multiplication in self-powered near-ultraviolet γ-InSe/graphene heterostructure photodetector with external quantum efficiency exceeding 161%. *Nano Lett.* **2024**, *24*, 7252–7260.

[37] He, S. X.; Feng, P.; Du, Y.; Ma, Y. P.; Dang, C. C.; Shan, A. D.; Zhao, L. C.; Wei, T. R.; Li, M.; Gao, L. M. High performance self-powered and vis-infrared broadband photodetectors based on $MoTe_2$/InSe van der Waals heterostructure. *Adv. Opt. Mater.* **2024**, *12*, 2302399.

[38] Zhu, Y.; Chen, H. B.; Han, R. M.; Qin, H.; Yao, Z. Y.; Liu, H.; Ma, Y. F.; Wan, X. J.; Li, G. H.; Chen, Y. S. High-speed flexible near-infrared organic photodiode for optical communication. *Natl. Sci. Rev.* **2024**, *11*, nwad311.

[39] Liang, G. X.; Luo, Y. D.; Chen, S.; Tang, R.; Zheng, Z. H.; Li, X. J.; Liu, X. S.; Liu, Y. K.; Li, Y. F.; Chen, X. Y. et al. Sputtered and selenized Sb_2Se_3 thin-film solar cells with open-circuit voltage exceeding 500 mV. *Nano Energy* **2020**, *73*, 104806.

[40] Chen, S.; Liu, T. X.; Chen, M. D.; Ishaq, M.; Tang, R.; Zheng, Z. H.; Su, Z. H.; Li, X. J.; Qiao, X.; Fan, P. et al. Crystal growth promotion and interface optimization enable highly efficient Sb_2Se_3 photocathodes for solar hydrogen evolution. *Nano Energy* **2022**, *99*, 107417.

[41] Gunawan, O.; Todorov, T. K.; Mitzi, D. B. Loss mechanisms in hydrazine-processed $Cu_2ZnSn(Se,S)_4$ solar cells. *Appl. Phys. Lett.* **2010**, *97*, 233506.

[42] Zhang, M.; Yang, P. P.; Tao, W. Y.; Pang, X. G.; Su, Y. Y.; Peng, P.; Zheng, L.; Li, R. H.; Wang, S. X.; Huang, J. et al. NiFe Prussian blue analog cocatalyzed TiO_2/In_2S_3 type-II heterojunction for solar water splitting. *Energy Mater.* **2024**, *4*, 400028.

[43] Lai, C. Z.; Zhou, X. J.; Lei, M.; Liu, W. L.; Mu, X. K.; Li, C. L. Scissor g-C_3N_4 for high-density loading of catalyst domains in mesoporous thin-layer conductive network for durable Li–S batteries. *Energy Mater.* **2023**, *3*, 300025.

[44] Li, L.; Chen, H. Y.; Fang, Z. M.; Meng, X. Y.; Zuo, C. T.; Lv, M. L.; Tian, Y. Z.; Fang, Y.; Xiao, Z.; Shan, C. X. et al. An electrically modulated single-color/dual-color imaging photodetector. *Adv. Mater.* **2020**, *32*, 1907257.

[45] Luo, G.; Shi, J. L.; Deng, W.; Chang, Z. Z.; Lu, Z. J.; Zhang, Y. J.; Pan, R.; Jie, J. S.; Zhang, X. J.; Zhang, X. H. Boosting the performance of organic photodetectors with a solution-processed integration circuit toward ubiquitous health monitoring. *Adv. Mater.* **2023**, *35*, 2301020.

[46] Zhao, Z. J.; Xu, C. Y.; Niu, L. B.; Zhang, X. L.; Zhang, F. J. Recent progress on broadband organic photodetectors and their applications. *Laser Photonics Rev.* **2020**, *14*, 2000262.

[47] Zhu, H.; Yu, H. W.; Zhang, J. M.; Zhang, Y. Q.; Zhang, L. T.; Liu, S. H.; Xie, W. F. Organic photoplethysmography sensor based on directional emission microcavity organic light-emitting device. *Laser Photonics Rev.* **2024**, *18*, 2400042.

[48] Zhao, Z. J.; Liu, B. Q.; Xie, C. L.; Ma, Y.; Wang, J.; Liu, M.; Yang, K. X.; Xu, Y. H.; Zhang, J.; Li, W. W. et al. Highly sensitive, sub-microsecond polymer photodetectors for blood oxygen saturation testing. *Sci. China Chem.* **2021**, *64*, 1302–1309.

[49] He, L. J.; Hu, G. J.; Jiang, J. Z.; Wei, W.; Xue, X. Z.; Fan, K.; Huang, H. T.; Shen, L. Highly sensitive tin-lead perovskite photodetectors with over 450 days stability enabled by synergistic engineering for pulse oximetry system. *Adv. Mater.* **2023**, *35*, 2210016.

[50] Lochner, C. M.; Khan, Y.; Pierre, A.; Arias, A. C. All-organic optoelectronic sensor for pulse oximetry. *Nat. Commun.* **2014**, *5*, 5745.

清华大学出版社 Tsinghua University Press | SciOpen